Eur. Phys. J. Spec. Top.
https://doi.org/10.1140/epjs/s11734-025-02074-0

THE EUROPEAN PHYSICAL JOURNAL SPECIAL TOPICS

Regular Article

Evaluating directionality via cross-predictability and cloud size ratio methods: application to cerebrovascular dynamic interactions during active orthostatism

Alberto Porta[1,2,a], Beatrice Cairo[1], Pavandeep Singh[2], Martina Anguissola[2], Chiara Arduino[2], Beatrice De Maria[3], Marco Ranucci[2], and Vlasta Bari[1,2]

[1] Department of Biomedical Sciences for Health, University of Milan, 20133 Milan, Italy
[2] Department of Cardiothoracic, Vascular Anesthesia and Intensive Care, IRCCS Policlinico San Donato, 20097 Milan, San Donato Milanese, Italy
[3] IRCCS Istituti Clinici Scientifici Maugeri, 20138 Milan, Italy

Received 20 May 2025 / Accepted 18 November 2025

Abstract We compare two different strategies for the evaluation of directionality based on state space correspondence (SSC) class, namely k-nearest neighbor cross-predictability (CP) and cloud size ratio (CSR) methods in the context of bivariate data. Several CSR approaches were considered. The techniques were applied to describe statistical dependences between mean arterial pressure (MAP) and mean cerebral blood velocity (MCBv) in 27 healthy volunteers (age: 44 ± 11 years; 14 females, 13 males) undergoing recordings at rest in the supine position (REST) and during active standing (STAND). A surrogate data approach was applied to check the null hypothesis of the absence of coupling. Over synthetic bivariate series generated by nonlinear stochastic interacting systems we found that only the CP technique was able to detect causality from the driver to the responder, while the performance of the CSR strategy was more limited. Over experimental data, we found that: (i) indexes computed via CP and CSR methods were significantly correlated, but correlation was weaker from MAP to MCBv; (ii) at REST closed loop MCBv-MAP dynamic interactions were detectable and they were more present during STAND; (iii) STAND increased the strength of the causal link from MAP to MCBv and vice versa. We conclude that the CP approach is more powerful than the CSR strategy in describing directionality of dynamic interactions even though values of the strength of the coupling computed by the two approaches are correlated and useful to describe the closed loop dependences between MAP and MCBv and the impact of the orthostatic challenge on them.

1 Introduction

The topic of assessing interactions between nonlinear dynamic systems X and Y attracts the interest of researchers from several fields, being the atom of the description of dependences among much more numerous entities [1]. Among the classes of methods usually utilized to assess the strength of the dynamic interactions between X and Y, the state space correspondence (SSC) class has been commonly applied since its early appearance [2]. The main feature of the SSC class is the reconstruction of the dynamic behavior of X and Y into two separate phase spaces via the delay embedding procedure and the characterization of the function mapping the embedding space of one system onto that of the other only grounded on the data, namely without imposing any a priori defined model [2]. The assumption is that close points in the reconstructed behavior of X correspond to close points in the reconstructed dynamics of Y via the estimated functional relationship [2]. The SSC class was found useful to quantify the strength of the relationship between X and Y [2–4]. The interest in the SSC methods rose dramatically when it was suggested that they can describe causality in a stimulus–response relationship [5–23]. Remarkably, the SSC class is a model-free causality method that does not follow much more dominant and universally accepted paradigms like those based on predictability improvement [24] or uncertainty decrement [25] about the behavior of the responder when the activity of the driver is accounted for. Applications of SSC methods to assess the

[a] e-mail: alberto.porta@unimi.it (corresponding author)

directionality of the interactions have flourished in several fields comprising systems physiology [9, 10, 12, 23], neuroscience [6–8, 14, 17, 21, 22], and population dynamics [5, 11].

The most frequently adopted metrics for the detection of directionality of the interactions between X and Y are based on cross-predictability (CP) of the evolution of Y conditioned on the behavior of X assessed via k nearest neighbors (KNNs) [5–13]. However, an alternative approach exploiting KNNs but grounded on distances computed in the embedding spaces more than on predictability has been proposed [14–19]. Given a reference vector in the embedding space of the driver and the responder being linked via a mapping function, this approach is based on the computation of cloud size ratio (CSR) obtained by dividing the size of the clouds formed by the KNNs of the reference vector in the embedding space of the responder by that of the cloud formed by the images of the KNNs of the reference vector in the embedding space of the driver through the mapping function [14].

The aim of this study is to compare CP and CSR approaches to assess the directionality of the interactions. Several CSR strategies are considered by differentiating local and global approaches as well as by considering average or maximal cloud size. The approach was tested in healthy subjects undergoing the evaluation of cerebral autoregulation (CA) [26, 27] based on the assessment of coupling strength between mean arterial pressure (MAP) and mean cerebral blood flow (MCBF), approximated via mean cerebral blood velocity (MCBv) as assessed via a transcranial Doppler (TCD) device from the middle cerebral artery [28], at rest in the supine position (REST) and during active standing (STAND) [29, 30].

2 Methods

2.1 Generalities for the computation of SSC methods

Let us consider two dynamic systems X and Y described by the scalar stochastic processes $X = \{X_n,\, n = 1, \ldots, N\}$ and $Y = \{Y_n,\, n = 1, \ldots, N\}$ respectively, where X_n and Y_n are two stochastic variables at time n and N is the time horizon of the observation of X and Y. The dynamics of X and Y are reconstructed from two realizations $x = \{x_n,\, n = 1, \ldots, N\}$ and $y = \{y_n,\, n = 1, \ldots, N\}$ of X and Y respectively using the method of the delay coordinates from the series of m-dimensional vectors $\boldsymbol{x} = \left\{\boldsymbol{x}_n = \left[\, x_n \ldots x_{n-m+1} \,\right],\, n = m, \ldots, N\right\}$ and $\boldsymbol{y} = \left\{\boldsymbol{y}_n = \left[\, y_n \ldots y_{n-m+1} \,\right],\, n = m, \ldots, N\right\}$, where m is the embedding dimension. Since the delay is equal to 1, $\boldsymbol{x}_n$ and $\boldsymbol{y}_n$ are patterns extracted from x and y. $\boldsymbol{x}_{n+\tau_{xy}}$ and $\boldsymbol{y}_{n+\tau_{yx}}$ are formed by the concatenation of the future value, namely $x_{n+\tau_{xy}}$ and $y_{n+\tau_{yx}}$ respectively, with $\boldsymbol{x}_n$ and $\boldsymbol{y}_n$ respectively, where τ_{xy} the latency of the action from Y to X, and τ_{yx} the latency of the action from X to Y. We indicate with $f(\cdot)$ and $g(\cdot)$ the functions mapping the dynamic behavior of X onto Y and vice versa. We define $\boldsymbol{y}_{n+\tau_{yx}}$ the image of $\boldsymbol{x}_n$ through the $f(\cdot)$, and $\boldsymbol{x}_{n+\tau_{xy}}$ the image of $\boldsymbol{y}_n$ through the $g(\cdot)$. Given that the dynamic behavior of X and Y are reconstructed in two separate and independent embedding spaces, the approach that will be pursued in the following is typical of the SSC class [2, 12]. We assume that X is the driver, Y is the target and a causal relationship $X \rightarrow Y$ from X to Y exists, if close states in the embedding space of X are mapped through the $f(\cdot)$ onto close states in the embedding space of Y. We assume that $Y \rightarrow X$ holds as well if $g(\cdot)$ leads to the same situation when the role of X and Y is reversed. The strength of the link from X to Y is inferred by assessing the ability of vectors built over X to set the evolution of those built over Y. While reversing the role of X and Y, the link from Y to X can be estimated as well. The dominant direction of the interaction is defined as the one setting the stronger dependence. The distance of the vectors in the embedding spaces is evaluated via the Euclidean norm. In the CP technique the KNN approach is utilized to decide the points about the reference vector $\boldsymbol{x}_n$ to be mapped onto the embedding space of Y through the $f(\cdot)$. In the CSR technique the size of cell formed by the KNNs of $\boldsymbol{y}_{n+\tau_{yx}}$ is compared to that resulting from images of the KNNs of the reference vector $\boldsymbol{x}_n$ through the $f(\cdot)$. When the role between X and Y is reversed, the KNN approach is followed as well, while vectors in the embedding space of Y are mapped onto those built in the embedding space of X via the $g(\cdot)$. When searching the KNNs of a vector we excluded only the vector with coincident time index, usually referred to as self-match [3].

2.2 SSC approach based on CP

CP strategy agrees with the notion that, in the presence of a smooth function $f(\cdot)$ mapping the states of X onto Y, vectors built in the embedding space of X are useful to predict those built in the embedding space of Y [31, 32]. The CP method utilizes the KNNs of $\boldsymbol{x}_n$ in the embedding space of X to predict the future value $y_{n+\tau_{yx}}$ of $\boldsymbol{y}_n$. The prediction $\widehat{y}_{n+\tau_{yx}}$ of $y_{n+\tau_{yx}}$ is obtained as the weighted mean of the future component of the images of the KNNs of $\boldsymbol{x}_n$, where the weights are the natural exponential of the inverse of the distance of the KNNs of $\boldsymbol{x}_n$ from $\boldsymbol{x}_n$ [33]. The strength of the dependence of Y on X is quantified by the square correlation coefficient ρ^2 between the predicted series $\widehat{y}$ and y [33, 34]. ρ^2 is taken as the CP function (CPF) from X to Y ($\mathrm{CPF}_{X\rightarrow Y}$). A situation of full unpredictability corresponds to $\mathrm{CPF}_{X\rightarrow Y} = 0$, while perfect prediction leads to $\mathrm{CPF}_{X\rightarrow Y} = 1$. A

well-defined course of $\mathrm{CPF}_{X\to Y}$ with m is expected: indeed, at small m, the better unfolding of trajectories in the embedding space of X might prevail leading to an improvement of CP, while at larger m the erratic spreading of vectors in the embedding space of X, mainly due to noise, might increase the cell size formed by the KNNs of $\boldsymbol{x}_n$ and reduce the reliability of the predictor, thus reducing CP. The maximum of the $\mathrm{CPF}_{X\to Y}$ over m is taken as the CP index from X to Y ($\mathrm{CPI}_{X\to Y}$) [34, 35]. In the present study, the optimal embedding dimension m was searched in the range between 1 and 10.

2.3 SSC approaches based on CSR

CSR strategies agree with the notion that, in the presence of a smooth function $f(\cdot)$ mapping the states of X onto Y, close vectors in the embedding space of X corresponds to close vectors in the embedding space of Y [2]. Thus, the CSR function (CSRF) is defined [14] as

$$\mathrm{CSRF}^{\mathrm{lave}}_{X\to Y} = \langle \frac{A^Y_n}{A^{Y|X}_n} \rangle, \tag{1}$$

where A^Y_n is the square distance between $\boldsymbol{y}_{n+\tau_{yx}}$ and its KNNs in the embedding space of Y averaged over k, $A^{Y|X}_n$ is the square distance between $\boldsymbol{y}_{n+\tau_{yx}}$ and the images of the KNNs of $\boldsymbol{x}_n$ in the embedding space of Y averaged over k, and $\langle\cdot\rangle$ performs the average over n. $\mathrm{CSRF}^{\mathrm{lave}}_{X\to Y}$ is a measure of strength of the dependence of Y onto X. Indeed, if the KNNs of $\boldsymbol{y}_{n+\tau_{yx}}$ corresponds perfectly to the images of the KNNs of $\boldsymbol{x}_n$ in the embedding space of Y and this situation happens for any n, then $\mathrm{CSRF}^{\mathrm{lave}}_{X\to Y} = 1$, thus indicating a strong coupling from X to Y. Conversely, if the images of the KNNs of $\boldsymbol{x}_n$ in the embedding space of Y spread about $\boldsymbol{y}_{n+\tau_{yx}}$ and this situation is iterated over n, $\mathrm{CSRF}^{\mathrm{lave}}_{X\to Y}$ tends to 0, thus indicating a weak coupling from X to Y. The subscript lave is utilized to stress that the ratio $\frac{A^Y_n}{A^{Y|X}_n}$ is computed locally for any pattern built over the embedding space of Y of time index n and the distances were averaged over k. An alternative local measure is

$$\mathrm{CSRF}^{\mathrm{lmax}}_{X\to Y} = \langle \frac{M^Y_n}{M^{Y|X}_n} \rangle, \tag{2}$$

where M^Y_n is the square distance between $\boldsymbol{y}_{n+\tau_{yx}}$ and the farthest KNN of $\boldsymbol{y}_{n+\tau_{yx}}$ in the embedding space of Y, $M^{Y|X}_n$ is the square distance between $\boldsymbol{y}_{n+\tau_{yx}}$ and the farthest image of the KNNs of $\boldsymbol{x}_n$ in the embedding space of Y. The subscript lmax indicates that the ratio $\frac{M^Y_n}{M^{Y|X}_n}$ was computed locally as $\mathrm{CSRF}^{\mathrm{lave}}_{X\to Y}$ but, instead of computing the average distance over k as in (1), the maximum distance was computed. According to the definition of global and local indexes given in [36], correspondent global indexes are computed as

$$\mathrm{CSRF}^{\mathrm{gave}}_{X\to Y} = \frac{\langle A^Y_n \rangle}{\langle A^{Y|X}_n \rangle} \tag{3}$$

and

$$\mathrm{CSRF}^{\mathrm{gmax}}_{X\to Y} = \frac{\langle M^Y_n \rangle}{\langle M^{Y|X}_n \rangle}, \tag{4}$$

where at difference with (1) and (2), the numerator and the denominator of the ratio are calculated by considering quantities averaged over n. The subscripts gave and gmax remind that they are global indexes. All the CSRFs vary with m. Since, at difference with CPF, no procedure can be utilized to optimize m, they must be sampled at an arbitrary m. Indeed, the strategy exploited in CPF cannot be utilized in CSRF given that the erratic spreading of vectors in the embedding space of Y affect both the KNNs of $\boldsymbol{y}_{n+\tau_{yx}}$ and the images of the KNNs of $\boldsymbol{x}_n$ through the $f(\cdot)$, thus tending to a compensation instead of forming a maximum as in the case of the CPF. We selected an intermediate value of m, namely $m = 6$, to avoid a too small embedding dimension that might prevent to unfolding trajectories and a too high dimension corresponding to high-dimensional dynamics unrealistic in our application. The CSRF at $m = 6$ was taken as the CSR index (CSRI) and labeled $\mathrm{CSRI}^{\mathrm{lave}}_{X\to Y}$, $\mathrm{CSRI}^{\mathrm{lmax}}_{X\to Y}$, $\mathrm{CSRI}^{\mathrm{gave}}_{X\to Y}$, and $\mathrm{CSRI}^{\mathrm{gmax}}_{X\to Y}$.

2.4 Causality assessment based on SSC methods

$\mathrm{CPI}_{X\to Y}$ Was taken as an index of the strength of the causal relationship from X to Y [12]. In complete analogy with $\mathrm{CPI}_{X\to Y}$, the markers $\mathrm{CSRI}^{\mathrm{lave}}_{X\to Y}$, $\mathrm{CSRI}^{\mathrm{lmax}}_{X\to Y}$, $\mathrm{CSRI}^{\mathrm{gave}}_{X\to Y}$, and $\mathrm{CSRI}^{\mathrm{gmax}}_{X\to Y}$ were utilized to estimate the strength of the causal relationship from X to Y as well. When they were significantly larger than 0, we argue that $X \to Y$. By reversing the role of X and Y an analogous approach can be followed to compute the CPF from Y on X ($\mathrm{CPF}_{Y\to X}$) and CSRF from Y to X according to (1)–(4), namely $\mathrm{CSRI}^{\mathrm{lave}}_{Y\to X}$, $\mathrm{CSRI}^{\mathrm{lmax}}_{Y\to X}$, $\mathrm{CSRI}^{\mathrm{gave}}_{Y\to X}$, and $\mathrm{CSRI}^{\mathrm{gmax}}_{Y\to X}$. These indexes are taken as measures of the causal relationship from Y to X. A directionality index (DI) [37] based on CPI was defined as

$$\mathrm{DI}_{\mathrm{CPI}} = \mathrm{CPI}_{Y\to X} - \mathrm{CPI}_{X\to Y} \tag{5}$$

and a normalized DI (NDI) [38] as

$$\mathrm{NDI}_{\mathrm{CPI}} = \frac{\mathrm{CPI}_{Y\to X} - \mathrm{CPI}_{X\to Y}}{\mathrm{CPI}_{Y\to X} + \mathrm{CPI}_{X\to Y}}. \tag{6}$$

Similar definitions can be provided for DI based on CSRI. If DI, or NDI, was significantly larger than 0, we argue that $Y \to X$ is the dominant direction of causality. When computing indexes from Y to X attention should be paid to use τ_{xy} instead of τ_{yx} because latencies can be different and to avoid setting $\tau_{yx} = \tau_{yx} = 0$ [12]. If both $X \to Y$ and $Y \to X$ subsisted, then a closed loop relationship was detected, being the dominant direction of causality the one with greater CPI, or CSRI.

3 Simulations

A bivariate model describing the interactions between nonlinear stochastic systems [12] was exploited to test the performance of the methods in assessing causality. Each equation features a quadratic term accounting for the self-dependence of one system and a linear term representing cross-dependence on the activity of the other system disturbed by dynamic noise. The model is described by

$$X_n = a \cdot X^2_{n-1} + b \cdot Y_{n-1} + \Xi_n \tag{5}$$

$$Y_n = c \cdot Y^2_{n-1} + d \cdot X_{n-1} + \Theta_n,$$

where $a = c = 0.1$ and Ξ and Θ are Gaussian white noises with zero mean and unit variances. If $b = 0$ and $d \neq 0$, the directionality of the interactions is from X to Y and the model is in open loop. If $b \neq 0$ and $d \neq 0$, the directionality of the interactions is from X to Y and vice versa and the model is in closed loop. In the case of a closed loop relationship the prevalent causal direction depends on the $|b/d|$ ratio. Causality was modified by letting constant the value of b, while d was varied incrementally from 0 to 1.0 with 0.05 steps. The value of b was set to 0.0, − 0.3 and − 0.6. Thus, by increasing progressively d, we expected that the dominance of the causal direction from X to Y could be more probable. However, this tendency depended on the value of b as well, being more likely to observe the prevalence of the reverse causal direction when $|b|$ was higher.

4 Experimental protocol and data analysis

4.1 Experimental protocol to probe cerebrovascular control

The cohort was a subsample of a larger group of healthy individuals enrolled at the IRCCS Policlinico San Donato, San Donato Milanese, Italy, with the aim of characterizing modifications of CA with age and orthostatic challenge. The group comprised individuals within the lowest tertile of age of the entire database. We analyzed 27 healthy volunteers (age: 44 ± 11 years; 14 females, 13 males). The healthy condition of individuals was verified via self-declaration of the subjects and clinical screening based on electrocardiogram and echocardiogram examinations. Preparation of the subjects, characteristics of the facilities where experimental sessions took place, and instructions given to the subjects followed the standards of protocols assessing CA at the IRCCS Policlinico San Donato [29, 39]. We recorded noninvasive continuous finger arterial pressure (AP) by volume-clamp photoplethysmography (CNAP Monitor 500, CNSystems, Austria), and cerebral blood velocity (CBv) via a TCD device (Multi-Dop X,

DWL, San Juan Capistrano, CA, USA) from the right or left middle cerebral artery. Signals were sampled at 400 Hz. After instrumenting the subject, a period of stabilization of the physiological variables of 10 min was allowed before starting the acquisition session. Signals were acquired at REST for 10 min followed by STAND for an additional period of 10 min.

4.2 Construction of variability series and computation of SSC indexes

The nth MAP was computed between the $(n-1)$th and the nth diastolic points detected on the AP signal. The correspondent fiducial points on the CBv were utilized for the computation of MCBv from the CBv signal [29]. CPI and CSRI markers were computed with $X = \text{MAP}$ and $Y = \text{MCBv}$. After the application of linear detrending, MAP and MCBv series were normalized to have zero mean and unit variance. Since short-term regulatory mechanisms were under focus, we adopted $N = 256$ [40]. The parameter k was set to 20 according to our previous experience on the analysis of the short data sequences that suggest that k is about 8% of N, which could preserve the ability to describe locally the characteristics of the dynamics while limiting the variance of the indexes [9, 12, 35]. Time delay was set to 1 [9, 12, 35]. We leveraged a test based on the stability of the mean and variance to check stationarity [41]. If a randomly selected sequence did not pass the test, a new selection was carried out.

4.3 Testing the null hypothesis of uncoupling via surrogate data

We set the null hypothesis of uncoupling between X and Y via the generation of surrogate series from the original x and y by preserving their distribution and power spectral density but destroying their cross-correlation [42]. We exploited iteratively refined amplitude-adjusted Fourier transform-based approach [43] to build pairs of series with the same distribution as the original series, while power spectral densities were the best approximation according to the number of iterates (i.e., 100). This method substituted the phases of the Fourier transform of the original x and y series with realizations of uniformly distributed random processes ranging from 0 to 2π. The use of two independent sequences generated according to two different random seeds, made the two surrogate series fully uncoupled [44]. The length N of the series, being a power of 2, allowed us to speed up the construction of surrogate data via fast Fourier transform. We generated 100 surrogate pairs from any original couple. CPI and CSRI markers were computed over each set of surrogates and the 95th percentile was extracted. If the marker computed over the original series was above the 95th percentile of the CPI distribution built over surrogates, the null hypothesis of uncoupling was rejected and the alternative hypothesis, namely the series were significantly associated in the considered time direction, was accepted [45]. The percentage of subjects with a significant CPI, or CSRI, was monitored as well and indicated as %CPI and %CSRI. Both %CPI and %CSRI from X to Y ($\%\text{CPI}_{X\to Y}$ and $\%\text{CSRI}_{X\to Y}$) and vice versa ($\%\text{CPI}_{Y\to X}$ and $\%\text{CSRI}_{Y\to X}$) were computed.

4.4 Statistical analysis

Paired t test, or Wilcoxon signed rank test when appropriate, was applied to check the impact of STAND over all the model-free directional markers. The χ^2 test (McNemar's test) was applied to the proportion of subjects featuring the rejection of the null hypothesis of uncoupling. Statistical tests were applied to markers describing both the directions of the interaction, namely from MAP to MCBv and vice versa. After pooling together markers computed in a given temporal direction regardless of the experimental condition, linear regression analysis was carried out in the planes ($\text{CPI}_{\text{MAP}\to\text{MCBv}}$, $\text{CSRI}_{\text{MAP}\to\text{MCBv}}$) and ($\text{CPI}_{\text{MCBv}\to\text{MAP}}$, $\text{CSRI}_{\text{MCBv}\to\text{MAP}}$). Pearson product moment correlation coefficient r and type I error probability p were calculated. Statistical analysis was performed with a commercial statistical software (Sigmaplot v.14.0, Systat Software, San Jose, CA, USA). A $p < 0.05$ was always deemed as significant.

5 Results

5.1 Results over simulations

Figure 1 shows the trends of CPI (Fig. 1a–c) and CSRI (Fig. 1d–o) computed according to the different strategies, namely $\text{CSRI}^{\text{gave}}$ (Fig. 1d–f), $\text{CSRI}^{\text{gmax}}$ (Fig. 1g–i), $\text{CSRI}^{\text{lave}}$ (Fig. 1j–l) and $\text{CSRI}^{\text{lmax}}$ (Fig. 1m–o), evaluated over the simulated series as a function of d. Results are obtained with $b = 0.0$ (Fig. 1a, d, g, j, m), $b = -0.3$ (Fig. 1b, e, h, k, n), and $b = -0.6$ (Fig. 1c, f, i, l, o). $\text{CPI}_{X\to Y}$ and $\text{CSRI}_{X\to Y}$ are represented as black lines, while $\text{CPI}_{Y\to X}$ and $\text{CSRI}_{Y\to X}$ as red lines. The dashed line represents the mean, and the two solid lines correspond to two standard deviations about the mean computed over the 100 simulated pairs. $\text{CPI}_{X\to Y}$ increased progressive with d regardless of the value of b (Fig. 1a–c). Conversely, $\text{CPI}_{Y\to X}$ remained stable with d when $b = 0.0$ (Fig. 1a)

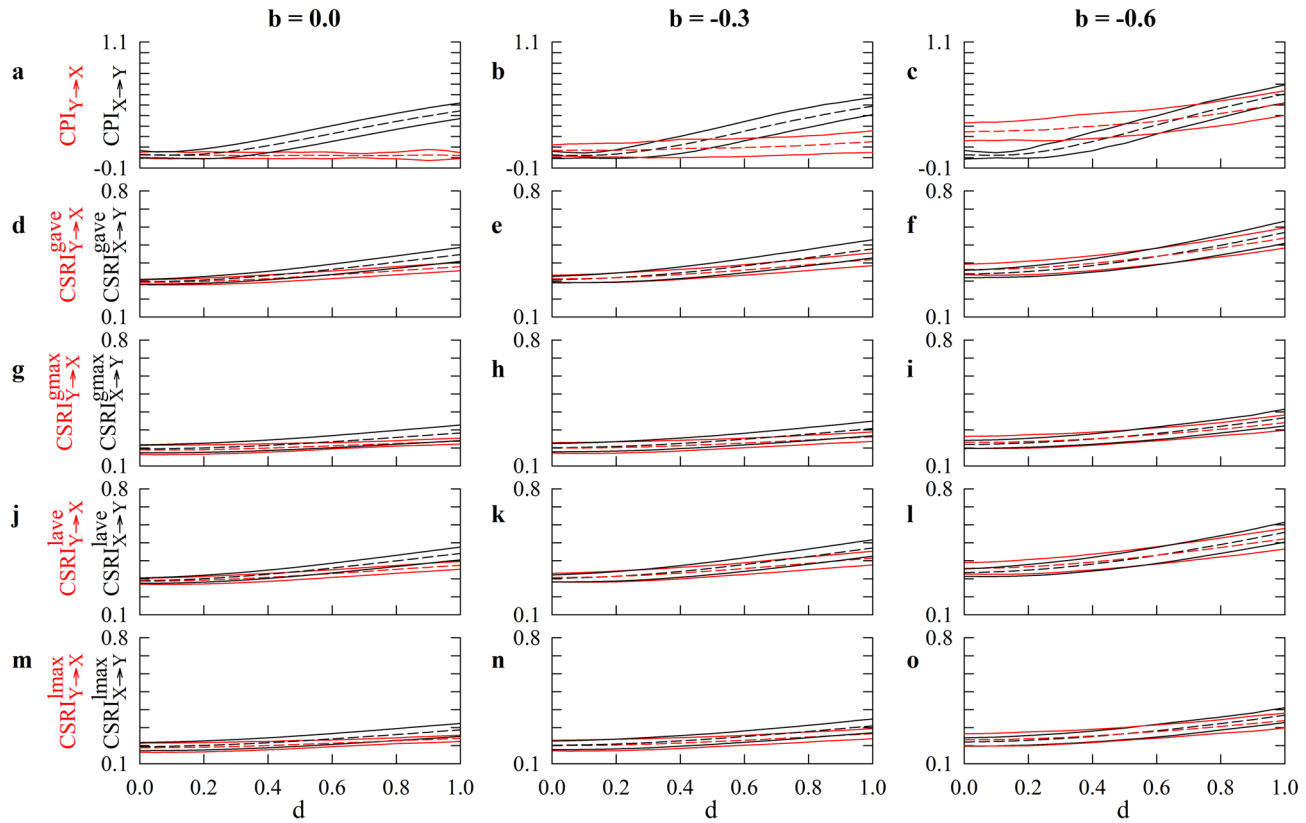

Fig. 1 The line plots show the mean (dashed line) and the confidence interval of two standard deviations about the mean (solid lines) of $\mathrm{CPI}_{X\to Y}$ (black lines) and $\mathrm{CPI}_{Y\to X}$ (red lines) in **a**–**c** and of $\mathrm{CSRI}_{X\to Y}$ (black lines) and $\mathrm{CSRI}_{Y\to X}$ (red lines) in **d**–**o** computed according to the strategy of the CSR approach, namely $\mathrm{CSRI}^{\mathrm{gave}}$ (**d**–**f**), $\mathrm{CSRI}^{\mathrm{gmax}}$ (**g**–**i**), $\mathrm{CSRI}^{\mathrm{lave}}$ (**j**–**l**), and $\mathrm{CSRI}^{\mathrm{lmax}}$ (**m**–**o**), assessed over simulated series with $a = c = 0.1$. Results are given as a function of d with $b = 0$ in (**a**, **d**, **g**, **j**, **m**), $b = -0.3$ in (b,e,h,k,n), and $b = -0.6$ in (**c**, **f**, **i**, **l**, **o**). The curves were built over 100 pairs of realizations of X and Y

and $b = -0.3$ (Fig. 1b), while it increased with d when $b = -0.6$ (Fig. 1c). $\mathrm{CPI}_{X\to Y}$ was above $\mathrm{CPI}_{Y\to X}$ at large d both when $b = 0.0$ and $b = -0.3$ (Figs.1a,b), while the reverse situation was observed at small d when $b = -0.6$ (Fig. 1c). Trends of $\mathrm{CSRI}_{X\to Y}$ and $\mathrm{CSRI}_{Y\to X}$ were very different from those of $\mathrm{CPI}_{X\to Y}$ and $\mathrm{CPI}_{Y\to X}$. Indeed, both of $\mathrm{CSRI}_{X\to Y}$ and $\mathrm{CSRI}_{Y\to X}$ increased progressively with d regardless of the strategy for their computation and the value of b (Fig. 1d–o), The consequence of these trends is that only at $b = 0.0$ $\mathrm{CSRI}_{X\to Y}$ was above $\mathrm{CSRI}_{Y\to X}$ at large d (Fig. 1a, d, g, j, m). Conversely, it is worth noting that it never happened that $\mathrm{CSRI}_{Y\to X}$ was above $\mathrm{CSRI}_{X\to Y}$. We conclude that CSRI is weaker than CPI in evaluating causality and it is suitable only in the case of unidirectional coupling.

5.2 Results over the experimental protocol

Figure 2 shows $\mathrm{CPI}_{\mathrm{MAP}\to\mathrm{MCBv}}$ (Fig. 2a) and $\%\mathrm{CPI}_{\mathrm{MAP}\to\mathrm{MCBv}}$ (Fig. 2b) at REST and during STAND. $\mathrm{CPI}_{\mathrm{MAP}\to\mathrm{MCBv}}$ increased significantly during STAND resulting in a significant rise of $\%\mathrm{CPI}_{\mathrm{MAP}\to\mathrm{MCBv}}$.

Figure 3 shows $\mathrm{CSRI}^{\mathrm{gave}}_{\mathrm{MAP}\to\mathrm{MCBv}}$ (Fig. 3a), $\mathrm{CSRI}^{\mathrm{gmax}}_{\mathrm{MAP}\to\mathrm{MCBv}}$ (Fig. 3c), $\mathrm{CSRI}^{\mathrm{lave}}_{\mathrm{MAP}\to\mathrm{MCBv}}$ (Fig. 3e), and $\mathrm{CSRI}^{\mathrm{lmax}}_{\mathrm{MAP}\to\mathrm{MCBv}}$ (Fig. 3g) as well as $\%\mathrm{CSRI}^{\mathrm{gave}}_{\mathrm{MAP}\to\mathrm{MCBv}}$ (Fig. 3b), $\%\mathrm{CSRI}^{\mathrm{gmax}}_{\mathrm{MAP}\to\mathrm{MCBv}}$ (Fig. 3d), $\%\mathrm{CSRI}^{\mathrm{lave}}_{\mathrm{MAP}\to\mathrm{MCBv}}$ (Fig. 3f), and $\%\mathrm{CSRI}^{\mathrm{lmax}}_{\mathrm{MAP}\to\mathrm{MCBv}}$ (Fig. 3h) at REST and during STAND. Regardless of the CSR method, $\mathrm{CSRI}_{\mathrm{MAP}\to\mathrm{MCBv}}$ raised during STAND (Fig. 3a, c, e, g) leading a tendency to augment $\%\mathrm{CSRI}_{\mathrm{MAP}\to\mathrm{MCBv}}$ (Fig. 3b, d, f, h) that was significant in the case of $\%\mathrm{CSRI}^{\mathrm{gmax}}_{\mathrm{MAP}\to\mathrm{MCBv}}$.

Figure 4 has the same structure as Fig. 2, but it shows CPI (Fig. 4a) and %CPI (Fig. 4b) computed over the reverse temporal direction, namely from MCBv to MAP. $\mathrm{CPI}_{\mathrm{MCBv}\to\mathrm{MAP}}$ increased significantly during STAND but $\%\mathrm{CPI}_{\mathrm{MCBv}\to\mathrm{MAP}}$ exhibited only a tendency to increase.

Figure 5 has the same structure as Fig. 3, but it shows CSRI (Fig. 5a, c, e, g) and %CSRI (Fig. 5b, d, f, h) over the reverse temporal direction, namely from MCBv to MAP. Regardless of the CSR method, $\mathrm{CSRI}_{\mathrm{MCBv}\to\mathrm{MAP}}$

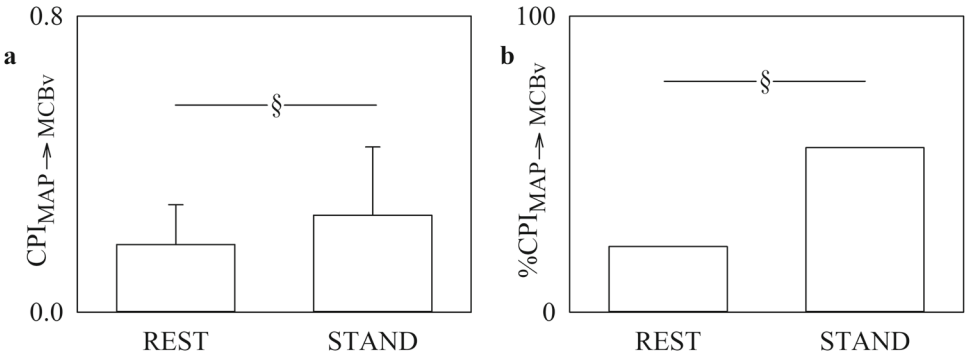

Fig. 2 The vertical error bar graph shows $\mathrm{CPI}_{\mathrm{MAP}\rightarrow\mathrm{MCBv}}$ (**a**) and the vertical bar graph shows $\%\mathrm{CPI}_{\mathrm{MAP}\rightarrow\mathrm{MCBv}}$ (**b**) as a function of the experimental condition (i.e., REST and STAND). Data in **a** are reported as mean + standard deviation and in **b** as percentage. The symbol § indicates $p < 0.05$ REST versus STAND

raised during STAND (Fig. 5a, c, e, g) but $\%\mathrm{CSRI}_{\mathrm{MCBv}\rightarrow\mathrm{MAP}}$ exhibited only a tendency to increase (Fig. 5b, d, f, h).

Figure 6 shows the results of linear regression analysis in the plane ($\mathrm{CPI}_{\mathrm{MAP}\rightarrow\mathrm{MCBv}}$, $\mathrm{CSRI}_{\mathrm{MAP}\rightarrow\mathrm{MCBv}}$) computed over all subjects after pooling together data relevant to REST and STAND. Analysis was carried using $\mathrm{CSRI}^{\mathrm{gave}}_{\mathrm{MAP}\rightarrow\mathrm{MCBv}}$ (Fig. 6a), $\mathrm{CSRI}^{\mathrm{gmax}}_{\mathrm{MAP}\rightarrow\mathrm{MCBv}}$ (Fig. 6b), $\mathrm{CSRI}^{\mathrm{lave}}_{\mathrm{MAP}\rightarrow\mathrm{MCBv}}$ (Fig. 6c), and $\mathrm{CSRI}^{\mathrm{lmax}}_{\mathrm{MAP}\rightarrow\mathrm{MCBv}}$ (Fig. 6d). $\mathrm{CPI}_{\mathrm{MAP}\rightarrow\mathrm{MCBv}}$ was significantly associated with $\mathrm{CSRI}^{\mathrm{gmax}}_{\mathrm{MAP}\rightarrow\mathrm{MCBv}}$ ($r = 0.270$, $p = 4.80 \times 10^{-2}$, Fig. 6b), $\mathrm{CSRI}^{\mathrm{lave}}_{\mathrm{MAP}\rightarrow\mathrm{MCBv}}$ ($r = 0.332$, $p = 1.40 \times 10^{-2}$, Fig. 6c), and $\mathrm{CSRI}^{\mathrm{lmax}}_{\mathrm{MAP}\rightarrow\mathrm{MCBv}}$ ($r = 0.317$, $p = 1.96 \times 10^{-2}$, Fig. 6d). Conversely, $\mathrm{CPI}_{\mathrm{MAP}\rightarrow\mathrm{MCBv}}$ was not significantly associated with $\mathrm{CSRI}^{\mathrm{gave}}_{\mathrm{MAP}\rightarrow\mathrm{MCBv}}$ ($r = 0.257$, $p = 6.08 \times 10^{-2}$, Fig. 6a).

Figure 7 has the same structure as Fig. 6, but it shows the results of linear regression in the plane ($\mathrm{CPI}_{\mathrm{MCBv}\rightarrow\mathrm{MAP}}$, $\mathrm{CSRI}_{\mathrm{MCBv}\rightarrow\mathrm{MAP}}$). $\mathrm{CPI}_{\mathrm{MCBv}\rightarrow\mathrm{MAP}}$ was significantly associated with $\mathrm{CSRI}_{\mathrm{MCBv}\rightarrow\mathrm{MAP}}$ regardless of the strategy of computation, namely with $\mathrm{CSRI}^{\mathrm{gave}}_{\mathrm{MCBv}\rightarrow\mathrm{MAP}}$ ($r = 0.630$, $p = 3.38 \times 10^{-7}$, Fig. 7a), $\mathrm{CSRI}^{\mathrm{gmax}}_{\mathrm{MCBv}\rightarrow\mathrm{MAP}}$ ($r = 0.608$, $p = 1.06 \times 10^{-5}$, Fig. 7b), $\mathrm{CSRI}^{\mathrm{lave}}_{\mathrm{MCBv}\rightarrow\mathrm{MAP}}$ ($r = 0.683$, $p = 1.26 \times 10^{-8}$, Fig. 7c) and $\mathrm{CSRI}^{\mathrm{lmax}}_{\mathrm{MCBv}\rightarrow\mathrm{MAP}}$ ($r = 0.636$, $p = 2.30 \times 10^{-7}$, Fig. 7d).

Figure 8 it shows $\mathrm{DI}_{\mathrm{CPI}}$ (Fig. 8a) and $\mathrm{NDI}_{\mathrm{CPI}}$ (Fig. 8b) at REST and during STAND. $\mathrm{DI}_{\mathrm{CPI}}$ and $\mathrm{NDI}_{\mathrm{CPI}}$ did not vary with STAND.

6 Discussion

The main findings can be summarized as follows: (i) synthetic bivariate data generated by a nonlinear stochastic model suggested that only the CP technique was able to detect causality from the driver to the responder, while the performance of CSR methods was more limited; (ii) in the context of cerebrovascular interactions CPI and CSRI were significantly correlated but the correlation was weaker from MAP to MCBv; (iii) at REST closed-loop MCBv-MAP dynamic interactions were detectable and they were more present during STAND; (iv) STAND increased the strength of the causal link from MAP to MCBv and vice versa.

6.1 The CP strategy is more powerful than the CSR one in describing causality in simulated nonlinear stochastic closed-loop dynamic interactions

Methods belonging to the SSC class were designed for characterizing the statistical relationship between two time series [2] and they were found useful to assess the directionality of dynamic interactions [5–23]. SSC methods can be mainly distinguished into two categories, namely based on CP [5–13] and CSR [14–19]. Both these families have been exploited to face the issue of distinguishing between the driver and the responder according to the asymmetry of the CP, or CSR, under reversal of the roles of the two series. Direct comparison of the two methods over simulations with the aim of assessing directionality is the missing piece of information given that the performance of CP and CSR strategies has been evaluated separately so far [5–13, 15–19]. In addition, separate validation was carried out mainly over deterministic systems and, when performed over stochastic systems, mainly in the presence of unidirectional coupling and/or with insufficient granularity of coupling strength [5–8, 10, 11, 13, 15, 16, 18, 19]. In the present study we directly compared the ability of CP and CSR in detecting driver-response directionality in the context of nonlinear stochastic closed-loop interactions. We found that the dominant direction

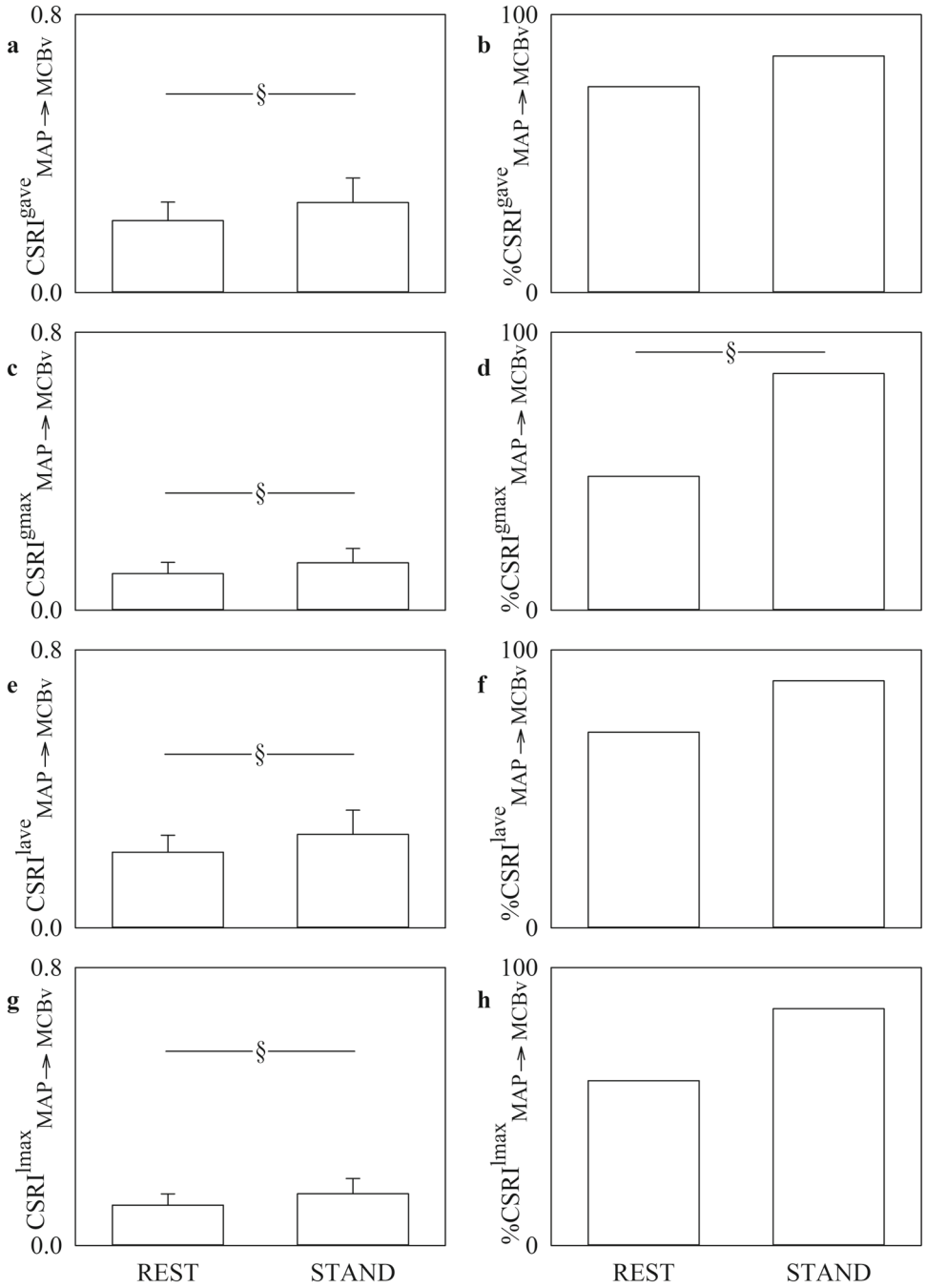

Fig. 3 The vertical error bar graphs show $\mathrm{CSRI}^{\mathrm{gave}}_{\mathrm{MAP}\rightarrow\mathrm{MCBv}}$ (**a**), $\mathrm{CSRI}^{\mathrm{gmax}}_{\mathrm{MAP}\rightarrow\mathrm{MCBv}}$ (**c**), $\mathrm{CSRI}^{\mathrm{lave}}_{\mathrm{MAP}\rightarrow\mathrm{MCBv}}$ (**e**), and $\mathrm{CSRI}^{\mathrm{lmax}}_{\mathrm{MAP}\rightarrow\mathrm{MCBv}}$ (**g**) and the vertical bar graphs show $\%\mathrm{CSRI}^{\mathrm{gave}}_{\mathrm{MAP}\rightarrow\mathrm{MCBv}}$ (**b**), $\%\mathrm{CSRI}^{\mathrm{gmax}}_{\mathrm{MAP}\rightarrow\mathrm{MCBv}}$ (**d**), $\%\mathrm{CSRI}^{\mathrm{lave}}_{\mathrm{MAP}\rightarrow\mathrm{MCBv}}$ (**f**), and $\%\mathrm{CSRI}^{\mathrm{lmax}}_{\mathrm{MAP}\rightarrow\mathrm{MCBv}}$ (**h**) as a function of the experimental condition (i.e., REST and STAND). Data in **a**, **c**, **e**, **g** are reported as mean + standard deviation and in **b**, **d**, **f**, **h** as percentage. The symbol § indicates $p < 0.05$ REST versus STAND

of the interactions was detected by the CP method as the one leading to the higher value of CP [12]. Conversely, the ability of CSR in detecting causality was weaker and limited to the ability to describe unidirectional interactions, namely with $b = 0.0$. We suggest that the worst performance of the CSR methods might be the result of the fact that the activity of the responder can be, at least partially, reconstructed from its past values without the need of knowing the activity of the driver. Indeed, this situation could have limited the differences between the cloud sizes formed by the neighbors of the state of the responder and by the images of the neighbors of the associated state in the embedding space of the driver. In other words, if the driver activity does not have an exclusive effect on the responder and the driver action could be reconstructed, even partially, from past states of the responder activity, causal relationships cannot be disentangled using the CSR methods examined in this study. Conversely, the CP approach leverages exclusively the KNNs detected in the embedding space of the driver to reconstruct the activity of the responder. Thus, we do not recommend the use of CSR methods to detect the dominant direction of causality in nonlinear stochastic closed-loop systems. As a consequence, we limited the analysis of directionality via DI to the CP method.

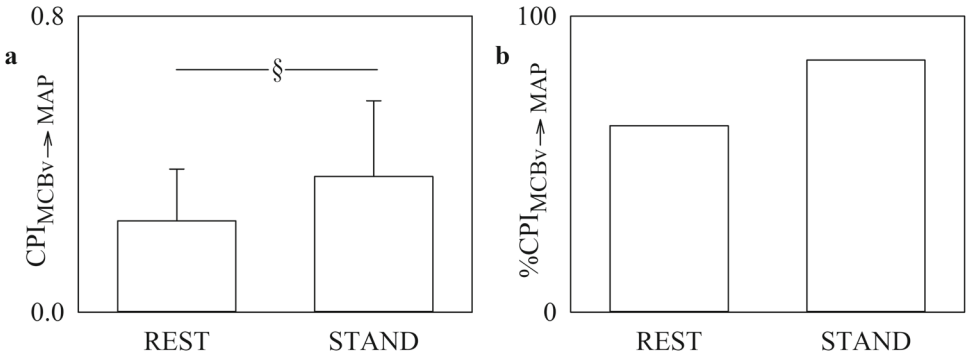

Fig. 4 The vertical error bar graph shows $CPI_{MCBv \rightarrow MAP}$ (**a**) and the vertical bar graph shows $\%CPI_{MCBv \rightarrow MAP}$ (**b**) as a function of the experimental condition (i.e., REST and STAND). Data in **a** are reported as mean + standard deviation and in **b** as percentage. The symbol § indicates $p < 0.05$ REST versus STAND

6.2 Correlation analysis between CPI and CSRI in the context of cerebrovascular dynamic interactions

Two factors might contribute to the significant correlation between CPI and CSRI. On the one hand CPI is computed via an optimization procedure leading to the selection of the embedding dimension allowing the best prediction of the behavior of the responder based on the activity of the driver, while the embedding dimension is a priori decided in the computation of CSRI. It might be that, if the variability of the optimal embedding dimension in CPI computation was limited, correlation would be high. Another factor that can contribute to the correlation between CPI and CSRI is the limited contribution of the past samples of the activity of the responder in setting its future evolution above and beyond the contribution of the driver. If the future behavior of the responder was completely governed by the activity of the driver, CPI and CSRI would be highly correlated. Indeed, while CPI depends exclusively on the activity of the driver, CSRI accounts for activity of the responder in addition to the behavior of the responder conditioned on the activity of the driver. The significant association between CPI and CSRIs indicates that the CSRIs can be exploited as a marker of coupling strength between interacting systems. Only $CSRI^{gave}_{MAP \rightarrow MCBv}$ was not significantly associated with $CPI_{MAP \rightarrow MCBv}$, but type I error probability is borderline to significance. However, in general, correlation is far from being high in the temporal direction from MAP to MCBv. We conclude that the variability of the optimal embedding dimension in the computation of CPI and the sizable contribution of past values of the activity of the responder in describing the action of the driver on the responder plays a role in limiting correlation between CPI and CSRI. This role appears to be more important from MAP to MCBv than in the reverse causal direction given that correlation between $CPI_{MAP \rightarrow MCBv}$ and $CSRI_{MAP \rightarrow MCBv}$ is weaker. We suggest that the complexity of the pathway from MAP to MCBv is so high, comprising endothelial, metabolic, chemical, neurogenic, and myogenic factors [46], that the pressure-to-flow pathway might provide a limited description of the dependence of cerebral fluid dynamics on AP changes [47], thus explaining the relevance assumed by the past samples of the MCBv in setting its future evolution above and beyond MAP variations. Conversely, the higher correlation between $CPI_{MCBv \rightarrow MAP}$ and $CSRI_{MCBv \rightarrow MAP}$ might be the result of the lower complexity of flow-to-pressure pathway responding to situations of hypo/hyperperfusion with suitable modification of MAP [48–50].

6.3 Significant closed loop interactions between MCBv and MAP are present at REST and they are more evident during STAND

Closed loop MCBv-MAP interactions were detected at REST. Indeed, the percentage of concomitant rejection of the null hypothesis of uncoupling over both the pressure-to-flow and flow-to-pressure pathways as detected by CPI was 19%, and much higher when considering $CSRI^{gave}$, $CSRI^{gmax}$, $CSRI^{lave}$, and $CSRI^{lmax}$, namely 52%, 30%, 48% and 30% respectively. Bidirectional MCBv-MAP interactions were more evident during STAND given the concomitant rejection of the null hypothesis of uncoupling over both the arms of the closed loop as measured via CPI, $CSRI^{gave}$, $CSRI^{gmax}$, $CSRI^{lave}$, and $CSRI^{lmax}$ rose to 48%, 70%, 67%, 74% and 70% respectively. The identification of a closed loop relationship between MAP and MCBv is not surprising [45, 49–51]. On the one hand, the arm from MAP to MCBv is the result of the vascular properties of the cerebral circulation shaping MCBv according to modifications of the MAP [47] and of CA reducing this dependence in the attempt to limit variability of MCBv [46], while on the other hand the arm from MCBv to MAP account for the possibility of modifying systemic AP based on the state of cerebral circulation [48] even in situations that are not life threatening [52, 53] and at time scales typical of short-term regulation [45, 49–51, 54, 55].

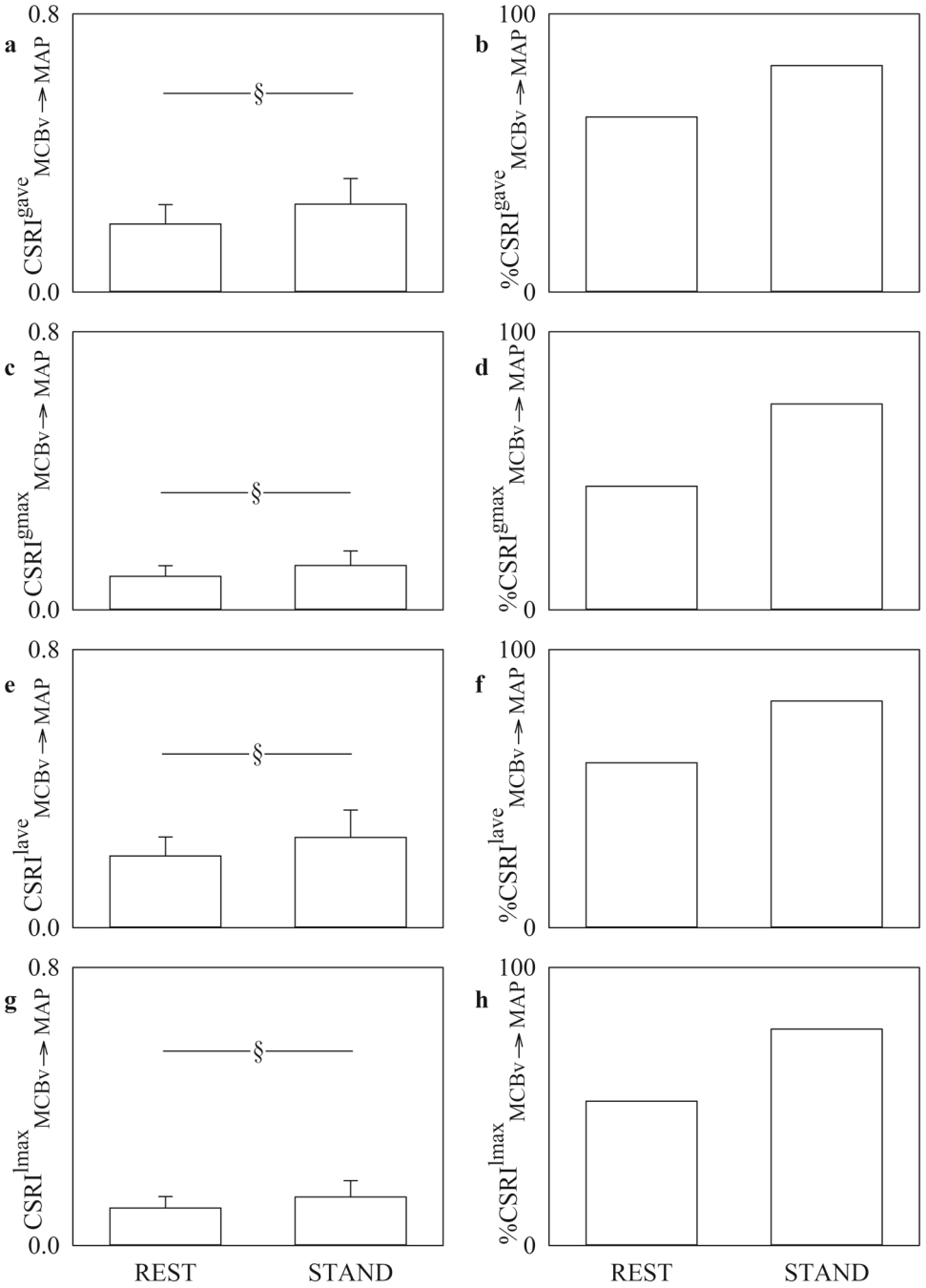

Fig. 5 The vertical error bar graphs show $CSRI^{gave}_{MCBv\rightarrow MAP}$ (**a**), $CSRI^{gmax}_{MCBv\rightarrow MAP}$ (**c**), $CSRI^{lave}_{MCBv\rightarrow MAP}$ (**e**), and $CSRI^{lmax}_{MCBv\rightarrow MAP}$ (**g**) and the vertical bar graphs show $\%CSRI^{gave}_{MCBv\rightarrow MAP}$ (**b**), $\%CSRI^{gmax}_{MCBv\rightarrow MAP}$ (**d**), $\%CSRI^{lave}_{MCBv\rightarrow MAP}$ (**f**), and $\%CSRI^{lmax}_{MCBv\rightarrow MAP}$ (**h**) as a function of the experimental condition (i.e., REST and STAND). Data in **a**, **c**, **e**, **g** are reported as mean + standard deviation and in **b**, **d**, **f**, **h** as percentage. The symbol § indicates $p < 0.05$ REST versus STAND

6.4 Both CPI and CSRI detect the deterioration of CA during STAND that might drive the activation of the flow-to-pressure pathway

Graded lower body negative pressure was utilized to simulate the impact of a reduced venous return typical of the orthostatic challenge [56, 57]. It was observed that the mean of MCBv decreased [56, 57], while the magnitude of the transfer function from MAP to MCBv as well as the strength of the association between MAP and MCBv band increased [57] in proportion to the relevance of the stressor. The impact of the postural challenge on the mean of MCBv [27, 49, 54, 58–62], and squared coherence in the very low and low frequency bands [9, 49, 62] was confirmed during head-up tilt and active standing in healthy subjects, thus supporting the deterioration of CA with the postural challenge. This deterioration was more visible in subjects prone to the development of postural syncope, especially in the temporal direction from MAP to MCBv [49, 54] and was evident when markers of CA were computed in the frequency domain especially in the high frequency band [45]. Conversely, the autoregulation index did not vary [27, 49, 59, 60] and it was even found to improve [61]. These modifications during postural stressors

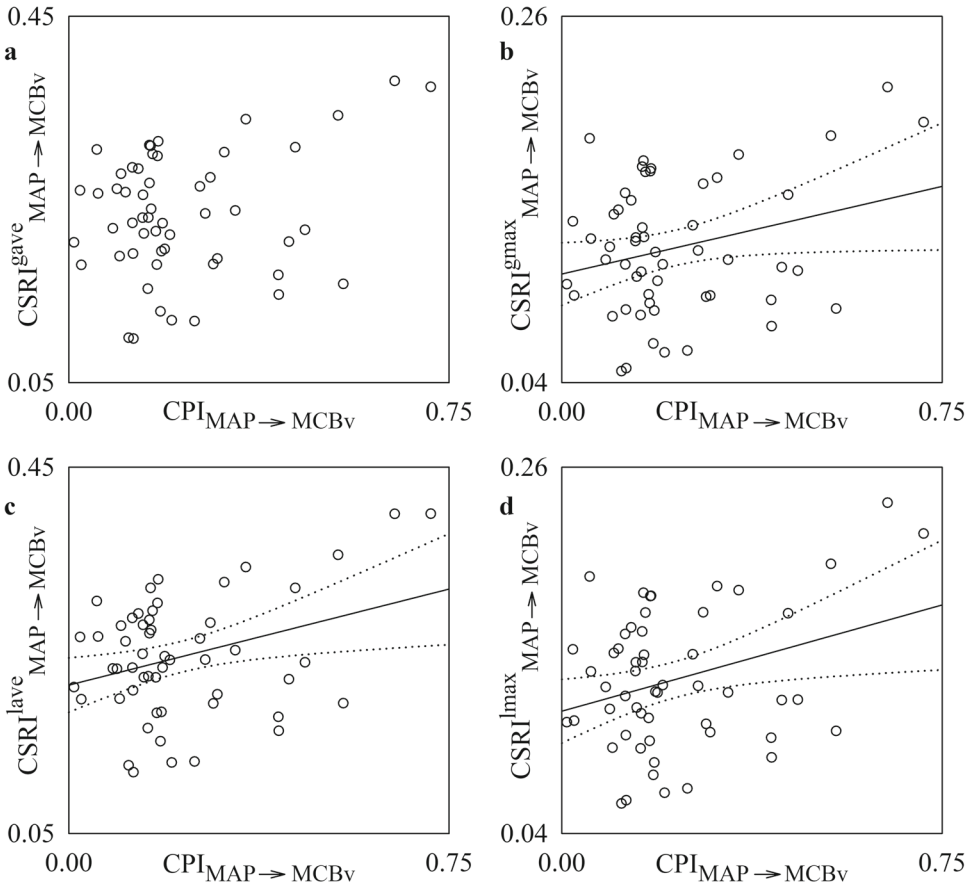

Fig. 6 Linear regression analysis in the plane ($CPI_{MAP\rightarrow MCBv}$, $CSRI_{MAP\rightarrow MCBv}$) computed over all the subjects is shown after pooling together all the data regardless of the experimental condition (i.e., REST or STAND). Analyses were made according to the strategy of the CSR approach, namely $CSRI^{gave}$ (**a**), $CSRI^{gmax}$ (**b**), $CSRI^{lave}$ (**c**), and $CSRI^{lmax}$ (**d**). Each open circle represents a pair of values computed over a subject in each experimental condition. The linear regression (solid line) and its 95% confidence interval (dotted lines) are plotted as well when association between the variables was significant with $p < 0.05$

have been interpreted as the result of vascular vasoconstriction at the cerebral level, being less important than that at the peripheral level but still present [56]. The present study agrees with the notion that an orthostatic challenge contributed to the deterioration of CA because the strength of the causal relationship from MAP to MCBv increased during STAND. This finding was more evident using CPI than CSRI given that the percentage of the subjects with a significant link from MAP to MCBv was more likely to increase with STAND. We argue that the increase in the strength of the causal relationship in the reverse temporal direction observed by both CPI and CSRI could be a physiological adjustment linked to the rise in the strength in the time direction from MAP to MCBv in the attempt to elicit suitable changes in MAP via Cushing-like reflexes to respond to situations of hypo/hyperperfusion [48–50, 55].

6.5 Limitations of the study and future developments

The embedding dimension m was optimized only by the CP method. Conversely, the CSR strategy relies on an arbitrary setting of m. Although in this study modifications of m did not alter conclusions, a procedure to optimize m in CSR methods would be warranted. However, to apply the same strategy adopted in the CP method the definition of CSR needs to be changed to prevent that dispersion of vectors influences both the numerator and denominator of CSR. Both CP and CSR approaches rely on the setting of the number k of the nearest neighbors. This number sets the level of coarse graining of the embedding space, being rougher with k. Indeed, higher values of k might lead to smooth local structures of the reconstructed dynamics. Strategies for selecting k according to the level of preservation of local structures might favor future applications. Even the application of coarse graining free approaches might deserve some tests [63, 64].

7 Conclusions

The CP method should be preferred to CSR strategies when assessing causality in a driver-response configuration featuring nonlinear stochastic interacting systems. This conclusion applies especially to those systems in which the

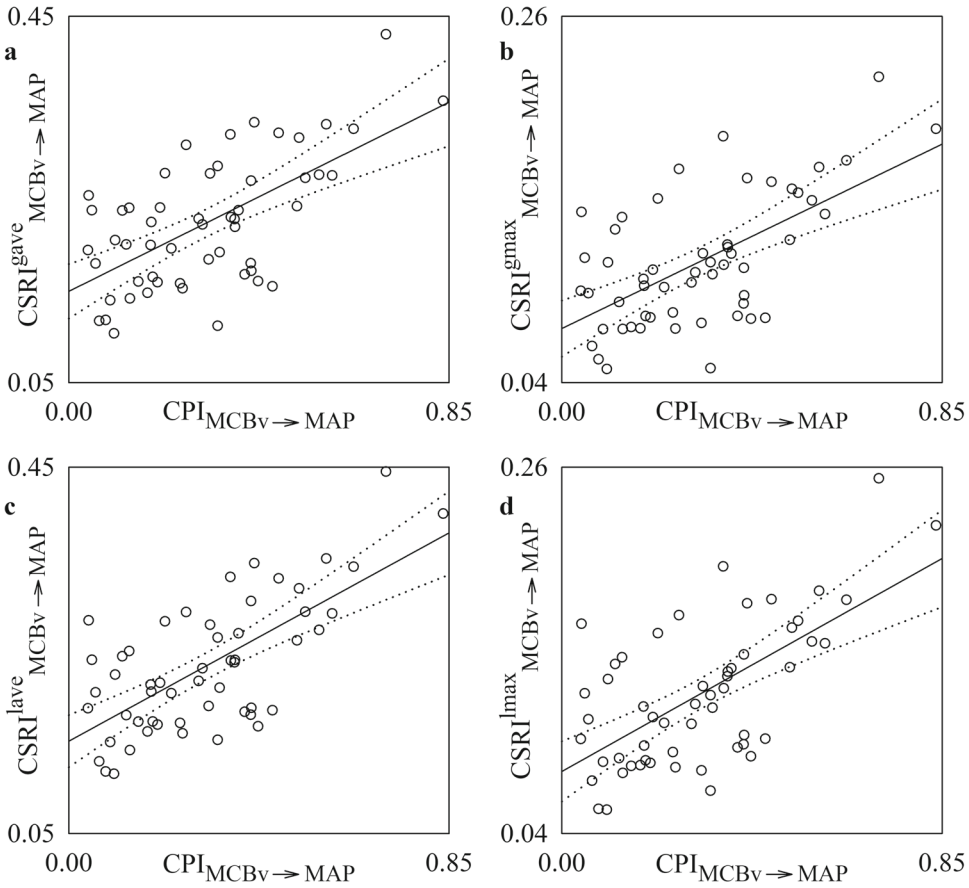

Fig. 7 Linear regression analysis in the plane ($CPI_{MCBv \rightarrow MAP}$, $CSRI_{MCBv \rightarrow MAP}$) computed over all the subjects is shown after pooling together all the data regardless of the experimental condition (i.e., REST or STAND). Analyses were made according to the strategy of the CSR approach, namely $CSRI^{gave}$ (**a**), $CSRI^{gmax}$ (**b**), $CSRI^{lave}$ (**c**), and $CSRI^{lmax}$ (**d**). Each open circle represents a pair of values computed over a subject in each experimental condition. The linear regression (solid line) and its 95% confidence interval (dotted lines) are plotted as well when association between the two variables is significant with $p < 0.05$

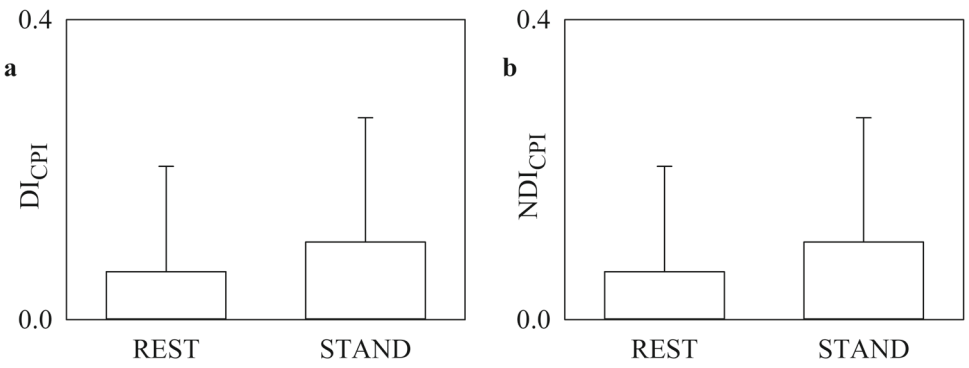

Fig. 8 The vertical error bar graphs show DI_{CPI} (**a**) and NDI_{CPI} (**b**) as a function of the experimental condition (i.e., REST and STAND). Data are reported as mean + standard deviation

impact of the driver on the responder does not appear to be the genuine effect of the driver but tends to inflate the contribution of past states of the responder to its future activity. However, the significant level of correlation between CPI and CSRI computed along the same temporal direction of interactions suggests that both methods are suitable to quantify the strength of the dynamic interactions between MAP and MCBv. Both methods suggest the presence of closed loop interactions between MAP and MCBv especially evident during STAND, thus stressing the pathophysiological relevance of the combined description of the pressure-to-flow and flow-to-pressure pathways. The ability of the SSC class to describe nonlinear directional interactions, its independence of any model structure, and its ability to detect changes across experimental conditions are all features that might be extremely useful in the characterization of the MAP-MCBv dynamic interactions as well as in the description of the relationship between any pair of physiological variables.

Author contributions

Alberto Porta: conceptualization; formal analysis; funding acquisition; investigation; methodology; resources; software; supervision; validation; visualization; writing—original draft; writing—review and editing. Beatrice Cairo: data curation; formal analysis; funding acquisition; investigation; writing—review and editing. Pavandeep Singh: data curation; investigation; writing—review and editing. Martina Anguissola: data curation; writing—review and editing. Chiara Arduino: writing—review and editing. Beatrice De Maria: writing—review and editing. Marco Ranucci: funding acquisition; resources; writing—review and editing. Vlasta Bari: data curation; formal analysis; funding acquisition; investigation; writing—review and editing.

Funding Open access funding provided by Università degli Studi di Milano within the CRUI-CARE Agreement. This work was partially supported by the Italian Ministry of University and Research (MUR) via the Progetto di Rilevante Interesse Nazionale (PRIN) 2022SLB5MX to Alberto Porta and by the Italian Ministry of Health via the Ricerca Corrente program to the IRCCS Policlinico San Donato.

Data availability The data are available from the corresponding author upon reasonable request.

Declarations

Conflict of interest The authors have no conflicts to disclose.

Ethical statement The study was performed according to the Declaration of Helsinki. All subjects gave their written informed consent. The study was approved by the ethical review board of the San Raffaele Hospital, Milan, Italy (approval number: 32/int/2020; approval date: 05/04/2020).

References

1. T. Stankovski, T. Pereira, P.V.E. McClintock, A. Stefanovska, Coupling functions: universal insights into dynamical interaction mechanisms. Rev. Mod. Phys. **89**, 045001 (2017). https://doi.org/10.1103/RevModPhys.89.045001
2. N.F. Rulkov, M.M. Sushchik, L.S. Tsimring, H.D.I. Abarbanel, Generalized synchronization of chaos in directionally coupled chaotic systems. Phys. Rev. E **51**, 980–994 (1995). https://doi.org/10.1103/PhysRevE.51.980
3. J.S. Richman, J.R. Moorman, Physiological time-series analysis using approximate entropy and sample entropy. Am. J. Physiol. Heart Circ. Physiol. **278**(6), H2039–H2049 (2000). https://doi.org/10.1152/ajpheart.2000.278.6.H2039
4. C.J. Stam, B.W. van Dijk, Synchronization likelihood: an unbiased measure of generalized synchronization in multivariate data sets. Phys. D **163**(3–4), 236–251 (2002). https://doi.org/10.1016/S0167-2789(01)00386-4
5. G. Sugihara, R. May, H. Ye, C. Hsieh, E. Deyle, M. Fogarty, S. Munch, Detecting causality in complex ecosystems. Science **338**(6106), 496–500 (2012). https://doi.org/10.1126/science.1227079
6. S.J. Schiff, P. So, T. Chang, R. Burke, T. Sauer, Detecting dynamical interdependence and generalized synchrony through mutual prediction in a neural ensemble. Phys. Rev. E **54**(6), 6708–6724 (1996). https://doi.org/10.1103/physreve.54.6708
7. M. Le Van Quyen, C. Adam, M. Baulac, J. Martinerie, F.J. Varela, Nonlinear interdependencies of EEG signals in human intracranially recorded temporal lobe seizures. Brain Res. **792**(1), 24–40 (1998). https://doi.org/10.1016/s0006-8993(98)00102-4
8. M. Le Van Quyen, J. Martinerie, C. Adam, F.J. Varela, Nonlinear analyses of interictal EEG map the brain interdependences in human focal epilepsy. Phys. D **127**(3–4), 250–266 (1999). https://doi.org/10.1016/S0167-2789(98)00258-9
9. A. Porta, V. Bari, F. Gelpi, B. Cairo, B. De Maria, D. Tonon, G. Rossato, L. Faes, On the different ability of cross-sample entropy and k-nearest-neighbor cross-unpredictability in assessing dynamic cardiorespiratory and cerebrovascular interactions. Entropy **25**(4), 599 (2023). https://doi.org/10.3390/e25040599
10. L. Faes, A. Porta, G. Nollo, Mutual non linear prediction as a tool to evaluate coupling strength and directionality in bivariate time series: comparison among different strategies based on k nearest neighbors. Phys. Rev. E **78**(2 Pt 2), 026201 (2008). https://doi.org/10.1103/PhysRevE.78.026201

11. J. Deng, B. Sun, N. Scheel, A.B. Renli, D.C. Zhu, D. Zhu, J. Ren, T. Li, R. Zhang, Causalized convergent cross-mapping and its approximate equivalence with directed information in causality analysis. PNAS Nexus **3**(1), pgad422 (2024). https://doi.org/10.1093/pnasnexus/pgad422
12. A. Porta, R.M. Abreu, V. Bari, F. Gelpi, B. De Maria, A.M. Catai, B. Cairo, On the validity of the state space correspondence strategy based on k-nearest neighbor cross-predictability in assessing directionality in stochastic systems: application to cardiorespiratory coupling estimation. Chaos **34**(5), 053115 (2024). https://doi.org/10.1063/5.0192645
13. A. Krakovska, J. Jakubik, M. Chvostekova, D. Coufal, N. Jajcay, M. Palus, Comparison of six methods for the detection of causality in bivariate time series. Phys. Rev. E **97**, 042207 (2018). https://doi.org/10.1103/PhysRevE.97.042207
14. J. Arnhold, P. Grassberger, K. Lehnertz, C.E. Elger, A robust method for detecting interdependences: application to intracranially recorded EEG. Phys. D **134**(4), 419–430 (1999). https://doi.org/10.1016/S0167-2789(99)00140-2
15. R.Q. Quiroga, J. Arnhold, P. Grassberger, Learning driver-response relationships from synchronization patterns. Phys. Rev. E **61**(5 Pt A), 5142–5148 (2000). https://doi.org/10.1103/physreve.61.5142
16. A. Schmitz, Measuring statistical dependence and coupling of subsystems. Phys. Rev. E **62**, 7508 (2000). https://doi.org/10.1103/PhysRevE.62.7508
17. R.Q. Quiroga, A. Kraskov, T. Kreuz, P. Grassberger, Performance of different synchronization measures in real data: a case study on electroencephalographic signals. Phys. Rev. E **65**, 041903 (2002). https://doi.org/10.1103/PhysRevE.65.041903
18. R.G. Andrzejak, A. Kraskov, H. Stogbauer, F. Mormann, T. Kreuz, Bivariate surrogate techniques: necessity, strengths, and caveats. Phys. Rev. E **68**(6 Pt 2), 066202 (2003). https://doi.org/10.1103/PhysRevE.68.066202
19. D. Chicharro, R.G. Andrzejak, Reliable detection of directional couplings using rank statistics. Phys. Rev. E **80**(2 Pt 2), 026217 (2009). https://doi.org/10.1103/PhysRevE.80.026217
20. C.M. Romano, M. Thiel, J. Kurths, C. Grebogi, Estimation of the direction of the coupling by conditional probability of recurrence. Phys. Rev. E **76**(3 Pt 2), 036211 (2007). https://doi.org/10.1103/PhysRevE.76.036211
21. K. Schiecke, B. Pester, D. Piper, F. Benninger, M. Feucht, L. Leistritz, H. Witte, Nonlinear directed interactions between HRV and EEG activity in children with TLE. IEEE Trans. Biomed. Eng. **63**(12), 2497–2504 (2016). https://doi.org/10.1109/TBME.2016.2579021
22. K. Schiecke, A. Schumann, F. Benninger, M. Feucht, K.-J. Baer, P. Schlattmann, Brain–heart interactions considering complex physiological data: processing schemes for time-variant, frequency-dependent, topographical and statistical examination of directed interactions by convergent cross mapping. Physiol. Meas. **40**(11), 114001 (2019). https://doi.org/10.1088/1361-6579/ab5050
23. R. Fadil, A.X.A. Huether, A.K. Verma, R. Brunnemer, A.P. Blaber, J.-S. Lou, K. Tavakolian, Effect of Parkinson's disease on cardio-postural coupling during orthostatic challenge. Front. Physiol. **13**, 863877 (2022). https://doi.org/10.3389/fphys.2022.863877
24. C.W.J. Granger, Testing for causality. A personal viewpoint. J. Econ. Dyn. Control **2**, 329–352 (1980). https://doi.org/10.1016/0165-1889(80)90069-X
25. R. Vicente, M. Wibral, M. Lindner, G. Pipa, Transfer entropy: a model-free measure of effective connectivity for the neurosciences. J. Comput. Neurosci. **30**(1), 45–67 (2011). https://doi.org/10.1007/s10827-010-0262-3
26. R. Zhang, J.H. Zuckerman, C.A. Giller, B.D. Levine, Transfer function analysis of dynamic cerebral autoregulation in humans. Am. J. Physiol. **274**(1 Pt 2), H233–H241 (1998). https://doi.org/10.1152/ajpheart.1998.274.1.h233
27. F. Gelpi, V. Bari, B. Cairo, B. De Maria, D. Tonon, G. Rossato, L. Faes, A. Porta, Dynamic cerebrovascular autoregulation in patients prone to postural syncope: comparison of techniques assessing the autoregulation index from spontaneous variability series. Auton. Neurosci. **237**, 102920 (2022). https://doi.org/10.1016/j.autneu.2021.102920
28. R. Aaslid, T.M. Markwalder, H. Nornes, Noninvasive transcranial Doppler ultrasound recording of flow velocity in basal cerebral arteries. J. Neurosurg. **57**(6), 769–774 (1982). https://doi.org/10.3171/jns.1982.57.6.0769
29. V. Bari, F. Gelpi, B. Cairo, M. Anguissola, S. Pugliese, B. De Maria, E.G. Bertoldo, V. Fiolo, E. Callus, C. De Vincentiis, M. Volpe, R. Molfetta, M. Ranucci, A. Porta, Characterization of cardiovascular and cerebrovascular controls via spectral causality analysis in patients undergoing surgical aortic valve replacement during a three-month follow-up. Physiol. Meas. **44**(9), 094001 (2023). https://doi.org/10.1088/1361-6579/acf992
30. F. Gelpi, V. Bari, B. Cairo, B. De Maria, R. Wells, M. Baumert, A. Porta, Evaluation of cardiovascular and cerebrovascular control mechanisms in postural orthostatic tachycardia syndrome via conditional transfer entropy: the impact of the respiratory signal type. Physiol. Meas. **44**(6), 064001 (2023). https://doi.org/10.1088/1361-6579/acdb47
31. J.D. Farmer, J.J. Sidorowich, Predicting chaotic time series. Phys. Rev. Lett. **59**, 845–848 (1987). https://doi.org/10.1103/PhysRevLett.59.845
32. H.D.I. Abarbanel, T.L. Carroll, L.M. Pecora, J.J. Sidorowich, L.S. Tsimring, Predicting physical variables in time-delay embedding. Phys. Rev. E **49**, 1840–1853 (1994). https://doi.org/10.1103/PhysRevE.49.1840
33. G. Sugihara, R.M. May, Non linear forecasting as a way of distinguishing chaos from measurement error in time series. Nature **344**(6268), 734–741 (1990). https://doi.org/10.1038/344734a0
34. A. Porta, S. Guzzetti, R. Furlan, T. Gnecchi-Ruscone, N. Montano, A. Malliani, Complexity and nonlinearity in short-term heart period variability: comparison of methods based on local nonlinear prediction. IEEE Trans. Biomed. Eng. **54**(1), 94–106 (2007). https://doi.org/10.1109/TBME.2006.883789
35. A. Porta, L. Faes, V. Bari, A. Marchi, T. Bassani, G. Nollo, N.M. Perseguini, J. Milan, V. Minatel, A. Borghi-Silva, A.C.M. Takahashi, A.M. Catai, Effect of age on complexity and causality of the cardiovascular control: comparison

between model-based and model-free approaches. PLoS ONE **9**(2), e89463 (2014). https://doi.org/10.1371/journal.pone.0089463
36. A. Porta, V. Bari, B. De Maria, B. Cairo, E. Vaini, M. Malacarne, M. Pagani, D. Lucini, On the relevance of computing a local version of sample entropy in cardiovascular control analysis. IEEE Trans. Biomed. Eng. **66**(3), 623–631 (2019). https://doi.org/10.1109/TBME.2018.2852713
37. M. Palus, A. Stefanovska, Direction of coupling from phases of interacting oscillators: an information-theoretic approach. Phys. Rev. E **67**, 055201 (2003). https://doi.org/10.1103/PhysRevE.67.055201
38. M.G. Rosenblum, A. Pikovsky, Detecting direction of coupling in interacting oscillators. Phys. Rev. E **63**, 045202 (2001). https://doi.org/10.1103/PhysRevE.64.045202
39. V. Bari, F. Gelpi, B. Cairo, M. Anguissola, E. Acerbi, M. Squillace, B. De Maria, E.G. Bertoldo, V. Fiolo, E. Callus, C. De Vincentiis, F. Bedogni, M. Ranucci, A. Porta, Impact of surgical aortic valve replacement and transcatheter aortic valve implantation on cardiovascular and cerebrovascular controls: a pilot study. Physiol. Rep. **12**(17), e70028 (2024). https://doi.org/10.14814/phy2.70028
40. Task Force of the European Society of Cardiology and the North American Society of Pacing and Electrophysiology, Heart rate variability—standards of measurement, physiological interpretation and clinical use. Circulation **93**(5), 1043–1065 (1996) https://doi.org/10.1161/01.CIR.93.5.1043
41. V. Magagnin, T. Bassani, V. Bari, M. Turiel, R. Maestri, G.D. Pinna, A. Porta, Non-stationarities significantly distort short-term spectral, symbolic and entropy heart rate variability indexes. Physiol. Meas. **32**(11), 1775–1786 (2011). https://doi.org/10.1088/0967-3334/32/11/S05
42. D. Prichard, J. Theiler, Generating surrogate data from time series with several simultaneously variables. Phys. Rev. Lett. **73**(7), 951–954 (1994). https://doi.org/10.1103/PhysRevLett.73.951
43. T. Schreiber, A. Schmitz, Improved surrogate data for nonlinearity tests. Phys. Rev. Lett. **77**, 635–638 (1996). https://doi.org/10.1103/PhysRevLett.77.635
44. M. Palus, Detecting phase synchronisation in noisy systems. Phys. Lett. A **235**(4), 341–351 (1997). https://doi.org/10.1016/S0375-9601(97)00635-X
45. A. Porta, F. Gelpi, V. Bari, B. Cairo, B. De Maria, D. Tonon, G. Rossato, L. Faes, Concomitant evaluation of cardiovascular and cerebrovascular controls via Geweke spectral causality to assess the propensity to postural syncope. Med. Biol. Eng. Comput. **61**(12), 3141–3157 (2023). https://doi.org/10.1007/s11517-023-02885-0
46. C.K. Willie, Y.C. Tzeng, J.A. Fisher, P.N. Ainslie, Integrative regulation of human brain blood flow. J. Physiol. **592**(5), 841–859 (2014). https://doi.org/10.1113/jphysiol.2013.268953
47. Y.C. Tzeng, B.A. MacRae, P.N. Ainslie, G.S.H. Chan, Fundamental relationships between blood pressure and cerebral blood flow in humans. J. Appl. Physiol. **117**(9), 1037–1048 (2014). https://doi.org/10.1152/japplphysiol.00366.2014
48. F.D. McBryde, S.C. Malpas, J.F.R. Paton, Intracranial mechanisms for preserving brain blood flow in health and disease. Acta Physiol (Oxf.) **219**(1), 274–287 (2017). https://doi.org/10.1111/apha.12706
49. V. Bari, B. De Maria, C.E. Mazzucco, G. Rossato, D. Tonon, G. Nollo, L. Faes, A. Porta, Cerebrovascular and cardiovascular variability interactions investigated through conditional joint transfer entropy in subjects prone to postural syncope. Physiol. Meas. **38**(5), 976–991 (2017). https://doi.org/10.1088/1361-6579/aa638c
50. S. Saleem, P.D. Teal, C.A. Howe, M.M. Tymko, P.N. Ainslie, Y.C. Tzeng, Is the Cushing mechanism a dynamic blood pressure-stabilizing system? Insights from Granger causality analysis of spontaneous blood pressure and cerebral blood flow. Am. J. Physiol. Regul. Integr. Comp. Physiol. **315**(3), 484–495 (2018). https://doi.org/10.1152/ajpregu.00032.2018
51. E. Vaini, V. Bari, A. Fantinato, V. Pistuddi, B. Cairo, B. De Maria, M. Ranucci, A. Porta, Causality analysis reveals the link between cerebrovascular control and acute kidney dysfunction after coronary artery bypass grafting. Physiol. Meas. **40**(6), 064006 (2019). https://doi.org/10.1088/1361-6579/ab21b1
52. H. Cushing, Some experimental and clinical observations concerning states of increased intracranial tension. Am. J. Med. Sci. **124**(3), 375–400 (1902)
53. C.J. Dickinson, Reappraisal of the Cushing reflex: the most powerful neural blood pressure stabilizing system. Clin. Sci. **79**(6), 543–550 (1990). https://doi.org/10.1042/cs0790543
54. L. Faes, A. Porta, G. Rossato, A. Adami, D. Tonon, A. Corica, G. Nollo, Investigating the mechanisms of cardiovascular and cerebrovascular regulation in orthostatic syncope through an information decomposition strategy. Auton. Neurosci: Basic Clin. **178**(1–2), 76–82 (2013). https://doi.org/10.1016/j.autneu.2013.02.013
55. A. Porta, F. Gelpi, V. Bari, B. Cairo, B. De Maria, D. Tonon, G. Rossato, M. Ranucci, L. Faes, Categorizing the role of respiration in cardiovascular and cerebrovascular variability interactions. IEEE Trans. Biomed. Eng. **69**(6), 2065–2076 (2022). https://doi.org/10.1109/TBME.2021.3135313
56. B.D. Levine, C.A. Giller, L.D. Lane, J.C. Buckey, C.G. Blomqvist, Cerebral versus systemic hemodynamics during graded orthostatic stress in humans. Circulation **90**(1), 298–306 (1994). https://doi.org/10.1161/01.cir.90.1.298
57. R. Zhang, J.H. Zuckerman, B.D. Levine, Deterioration of cerebral autoregulation during orthostatic stress: insights from the frequency domain. J. Appl. Physiol. **85**(3), 1113–1122 (1998). https://doi.org/10.1152/jappl.1998.85.3.1113
58. B.P. Grubb, G. Gerard, K. Roush, P. Temesy-Armos, P. Montford, L. Elliott, H. Hahn, P. Brewster, Cerebral vasoconstriction during head-upright tilt-induced vasovagal syncope: a paradoxic and unexpected response. Circulation **84**(3), 1157–1164 (1991). https://doi.org/10.1161/01.cir.84.3.1157

59. B.J. Carey, B.N. Manktelow, R.B. Panerai, J.F. Potter, Cerebral autoregulatory responses to head-up tilt in normal subjects and patients with recurrent vasovagal syncope. Circulation **104**(8), 898–902 (2001). https://doi.org/10.1161/hc3301.094908
60. B.J. Carey, R.B. Panerai, J.F. Potter, Effect of aging on dynamic cerebral autoregulation during head-up tilt. Stroke **34**(8), 1871–1875 (2003). https://doi.org/10.1161/01.STR.0000081981.99908.F3
61. P. Castro, J. Freitas, R. Santos, R. Panerai, E. Azevedo, Indexes of cerebral autoregulation do not reflect impairment in syncope: insights from head-up tilt test of vasovagal and autonomic failure subjects. Eur. J. Appl. Physiol. **117**(9), 1817–1831 (2017). https://doi.org/10.1007/s00421-017-3674-1
62. V. Bari, L. Barbarossa, F. Gelpi, B. Cairo, B. De Maria, D. Tonon, G. Rossato, L. Faes, M. Ranucci, R. Barbieri, A. Porta, Exploring metrics for the characterization of the cerebral autoregulation during head-up tilt and propofol general anesthesia. Auton. Neurosci. **242**, 103011 (2022). https://doi.org/10.1016/j.autneu.2022.103011
63. C. Bandt, B. Pompe, Permutation entropy: a natural complexity measure for time series. Phys. Rev. Lett. **88**, 174102 (2002). https://doi.org/10.1103/PhysRevLett.88.174102
64. A. Porta, V. Bari, A. Marchi, B. De Maria, P. Castiglioni, M. Di Rienzo, S. Guzzetti, A. Cividjian, L. Quintin, Limits of permutation-based entropies in assessing complexity of short heart period variability. Physiol. Meas. **36**(4), 755–765 (2015). https://doi.org/10.1088/0967-3334/36/4/755